

# THESIS PROPOSAL

**Title:** Indirect measurement of cosmic-ray proton spectrum using Earth's  $\gamma$ -ray data from *Fermi* Large Area Telescope

**Student:** Patomporn Payoungkhamdee 6138171 SCPY/M

**Supervisor:** Assistance Professor Warit Mitthumsiri

**Degree:** Master's degree

**Field of study:** Physics

**Faculty of Science, Mahidol University**

## 1 Introduction

Cosmic-ray research has been pioneered by Theodor Wulf and Victor Hess who took electrometer measured cosmic ray from the ground to higher altitude and later experiment has confirmed that there are cosmic rays from outer space which can penetrate and interact with the Earth atmosphere [1–3].

There are many possible phenomena of acceleration mechanism in the space that could produce high energy particles. Consequently, characteristic of acceleration mechanism could roughly be distinguished by a spectral index in the arrival of cosmic ray spectrum in rigidity. Breaking point of the spectrum mainly comes from the overlapped region of acceleration mechanism that could be an evidence to explore a new candidate of acceleration type.

In 2011, PAMELA detector indicates that there is a break point of cosmic-ray proton spectrum around 240 GV [4]. Furthermore, AMS-02 also found a drastic change of proton CR spectrum at around 336 GV [5].

In this work, the indirect measurement of proton cosmic ray will be performed by using gamma-ray data from *Fermi* Large Area Telescope (*Fermi*-LAT).

## 2 Background knowledge

### 2.1 Cosmic rays

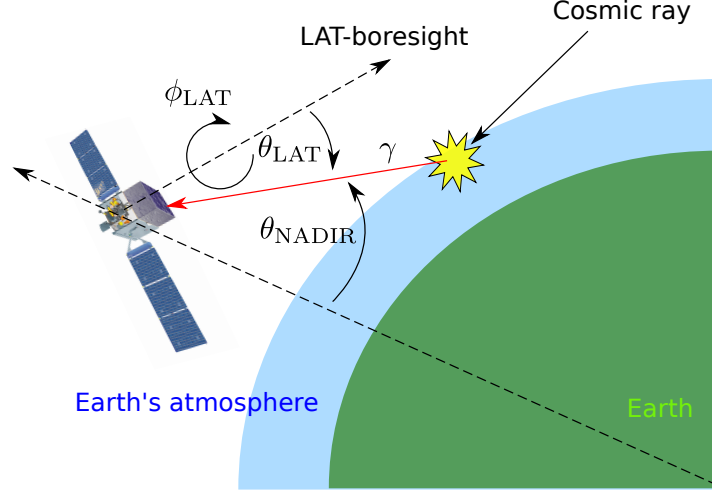


Figure 1: Schematic of  $\gamma$ -ray production

Cosmic rays (CRs) are high energy particles which are produced in space by various types of acceleration mechanisms such as supernovae, active galactic nuclei, quasars, and gamma-ray bursts. The main composition of CRs consist of 90% protons, 8% alpha and other heavier atoms. The widely accepted explanation why CR spectrum follows a power-law function in rigidity is that the acceleration mechanism was modeled as diffusive shock which has a characteristic spectral index.

The values of CR spectral indices vary for different ranges of energies, depending on the types of sources which can accelerate CRs to a certain energy range as shown in Figure 2 [6].

The motivation why we use  $\gamma$ -ray as a secondary product for investigate incident proton spectrum is that Earth limb's  $\gamma$ -ray relatively brigher than the sky due to collision from CRs in energy range 100 MeV and 1 TeV which consistent with our study [7].

Previous work has been performed using Pass 7 version data [8] and found an energy break point around 300 GeV with a significance of about  $2\sigma$  [9]. This result is consistent with direct measurements from [4, 5].

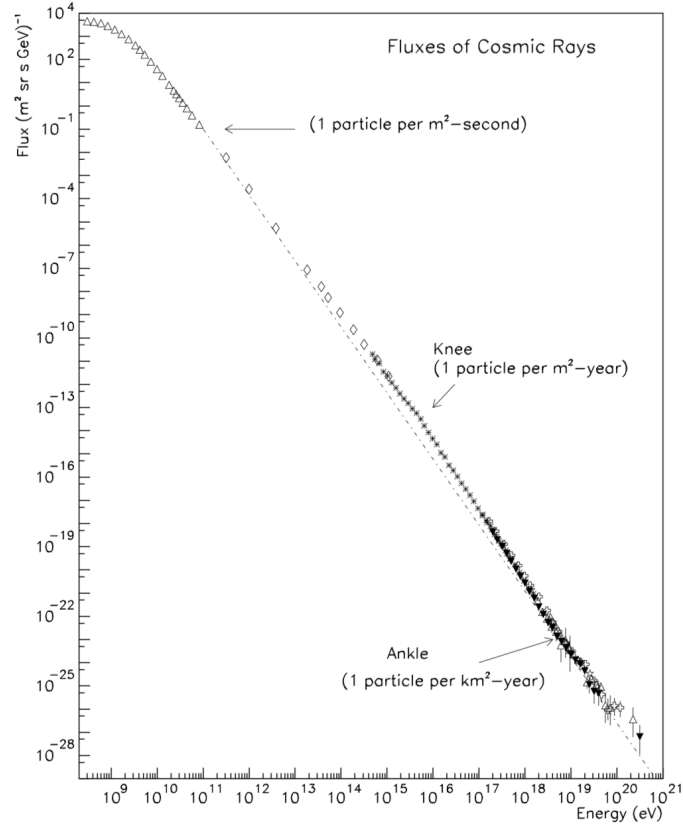


Figure 2: Main features of cosmic rays spectrum: Image taken from Swordy [6]

## 2.2 *Fermi* Large Area Telescope

Gamma-ray Large Area Space Telescope (GLAST) could be informally called *Fermi*-LAT. The mission is to collect data of particles from multiple phenomena such as active galaxy nuclei (AGN), pulsars and other high energy sources. It also attach the Gamma-ray Burst Monitor (GBM) to study gamma-ray bursts. Fermi was launched on 11 June 2008 at 16:05 UTC aboard a Delta II 7920-H rocket.

### Instrument

LAT consist with 16 layers of tracker (TKR) modules, 16 calorimeter (CAL) and a partition ACD.

TKR module has made from an array of silicon-strip tracking detectors (SSDs) and has 18 tracker on a horizontal planes. First 12 planes have 0.035 radiation lengths, next 4 laves contain 0.18 radiation lengths thick and the rest of it does not have any converter. Tracking detector in each plane consist of two planar inner layer which running in x and y axis subsequently. The arrival  $\gamma$ -ray in LAT's field of view could produce electron-positron pair in TKR's plates. The initial lepton pair could be determined from the recoed of conversion point in SSD planes with a power angular resolution when has a low energy.

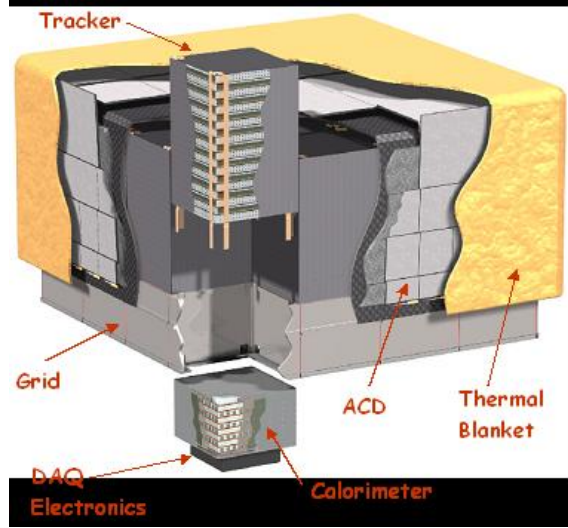


Figure 3: Instrument structure : Image taken from <https://fermi.gsfc.nasa.gov>

Each CAL module contains 1536 CsI(Tl) crystal with an 96 crystal align in eight different orthogonal layers. Dual PIN photodiodes also attach in each crystal which provide a great resolution in energy.

ACD tile contain wavelength shifting fiber by photomultiplier tubes (PMT) for redundancy. The tiles also are piled up in one direction.

## Event reconstruction

The methodology of detection is to track the lepton pair product from an incident photon that collide with a conversion foils and lepton product be traced by second inner layer of TKR. Consequently, the limit of precision depends on energy of photon that larger than mass energy of electron-positron as well as angle resolution of TKR that getting worse and worse at larger  $\theta_{LAT}$ . Lastly, the lepton product could be measured the energy by a high precision crystal array in CAL. The event classification also divided into various level of confident event reconstruction with a different Instrument response function [10, 11].

## 3 Methodology and Scope

### 3.1 Data sets

Photon data with a newest version of events reconstruction (would be last version) from *Fermi*-LAT

- P8R2\_ULTRACLEANVETO\_V6 data from 07/08/2008 to 16/10/2017 ( $\sim 9$

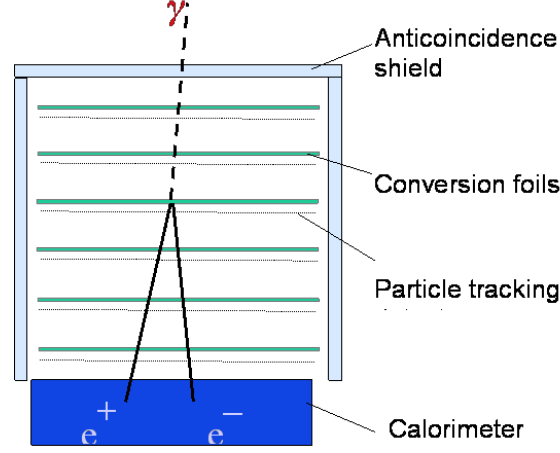


Figure 4: Structure of the LAT : Image taken from <https://fermi.gsfc.nasa.gov>

years)

- Collect photon energy range = 10 GeV to 1 TeV
- $\theta_{\text{NADIR}} = 68.4^\circ - 70^\circ$  (Earth's limb)
- Use  $\theta_{\text{LAT}} < 70^\circ$

Note that the reasons that we use ULTRACLEANVETO type of event reconstruction are it is the cleanest reconstruction catalogue.

### 3.2 Flux extraction

1. Reprocess photon data by taking into account
  - Treat photon energy bias 3.7% that be affected the energy range above 10 GeV
  - Adjust limb angle due to LAT altitude shift due to detection of  $\theta_{\text{Limb}}$  was tilt relatively to altitude of the spacecraft when orbit around asymmetric spherical Earth
2. Construct 2D histogram in Earth's angular coordinate ( $\theta_{\text{ZENITH}}$  and  $\phi_{\text{EARTH}}$ )
3. Fill photon data in different energy range
4. Calculate exposure maps which include effective area and time that LAT field of view can glimpse area of interest
5. Divide every single grid count map by exposure map
6. Sum over limb region of this map then divided by solidangle and energy bin width, then fill data in  $\gamma$ -ray energy spectrum as the formula 3.1

$$\text{Flux} \equiv \frac{dF}{dE} = \frac{\int_{\text{Limb region}} (\text{Count map/Exposure map})}{\Delta\Omega\Delta E} \quad (1)$$

7. Taking consider background subtraction from a average uniform background photon distribution by treating bin by bin

### 3.3 Coordinate Transformations

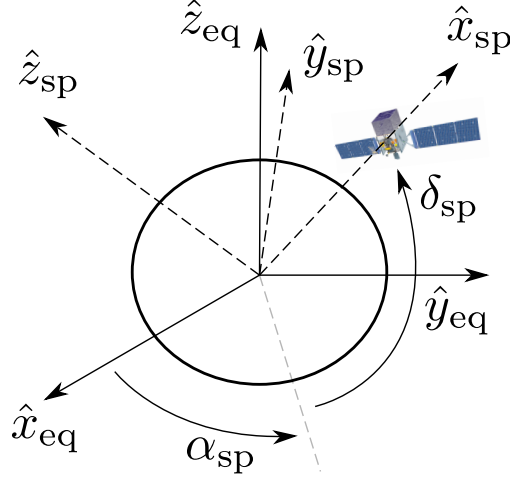


Figure 5: Coordinate transform between equatorial and spacecraft

$$\begin{aligned}
 \hat{x}_{sp} &= \cos \delta_{sp} \cos \alpha_{sp} \hat{x}_{eq} + \cos \delta_{sp} \sin \alpha_{sp} \hat{y}_{eq} + \sin \delta_{sp} \hat{z}_{eq} \\
 \hat{z}_{sp} &= -\sin \delta_{sp} \hat{y}_{eq} + \cos \delta_{sp} \hat{z}_{eq} \\
 \hat{y}_{sp} &= \hat{z}_{sp} \times \hat{x}_{sp}
 \end{aligned} \tag{2}$$

The transform matrix between equatorial coordinate and spacecraft coordinate could be represent as a relation in Eq 2

$$\hat{r}_{sp} \equiv T_{eq \rightarrow sp}(\delta_{sp}, \alpha_{sp}) \hat{r}_{eq} \tag{3}$$

$$\begin{aligned}
 \hat{x}_p &= \cos \delta_p^x \cos \alpha_p^x \hat{x}_{eq} + \cos \delta_p^x \sin \alpha_p^x \hat{y}_{eq} + \sin \delta_p^x \hat{z}_{eq} \\
 \hat{z}_p &= \cos \delta_p^z \cos \alpha_p^z \hat{x}_{eq} + \cos \delta_p^z \sin \alpha_p^z \hat{y}_{eq} + \sin \delta_p^z \hat{z}_{eq} \\
 \hat{y}_p &= \hat{z}_p \times \hat{x}_p
 \end{aligned} \tag{4}$$

According to Eq 4, the transformation matrix between LAT-boresight and equatorial coordinate could be derived from

$$\hat{r}_p \equiv T_{eq \rightarrow p}(\delta_p^x, \alpha_p^x, \delta_p^z, \alpha_p^z) \hat{r}_{eq} \tag{5}$$

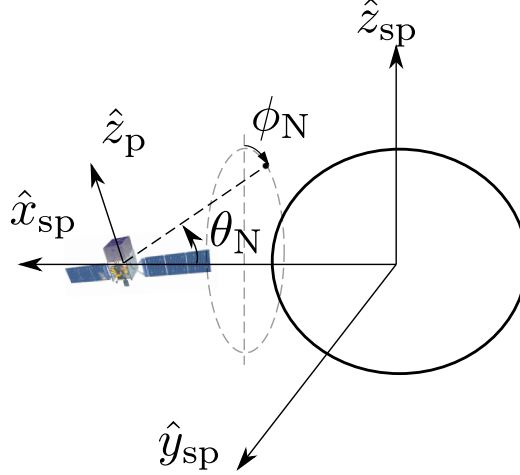


Figure 6: Coordinate transform between LAT-plane boresight and spacecraft

Importantly, the current status of lat field of view need to be consider in order to fill in the exposure map with the Earth's polar coordinate from satellite point of view as

$$\hat{r}_{sp}^o(\theta_N, \phi_N) \equiv -\cos \theta_N \hat{x}_{sp} + \sin \theta_N \cos \phi_N \hat{z}_{sp} + \sin \theta_N \sin \phi_N \hat{y}_{sp} \quad (6)$$

Since the spacecraft coordinate has already linked to the nadir's angle, the next step is to transform it into central coordinate which basically is the equatorial coordinate and convert it into LAT-boresight coordinate (Eq 7)

$$\hat{r}_p^o(\theta_N, \phi_N) = T_{eq \rightarrow p}(\delta_p^x, \alpha_p^x, \delta_p^z, \alpha_p^z) [T_{eq \rightarrow sp}(\delta_{sp}, \alpha_{sp})]^{-1} \hat{r}_{sp}^o(\theta_N, \phi_N) \quad (7)$$

Geometrically, angular coordinate of LAT plane could be obtained from normalized component of the cartesian unit vector as in Fig 7. The exposure accumulation has been calculated in every single grid from the previous relation.

The calculation of exposure map has to be done wisely one energy at a time due to the effective area of the spacecraft at each angle has various efficiency depends on the incident energy of gamma-ray as in the Fig 8. Under the condition of exposure-energy at a time, another factor that has to be consider carefully is the resolution of the exposure map. The higher resolution, the longer calculation time consumption which means we have to make  $\theta_N$  more precise than  $\phi_N$  because the limb region is more sensitive.

For both reasons, the first version of calculation takes approximately a month or more to finish. However, there is a plenty of room to improve. Here is

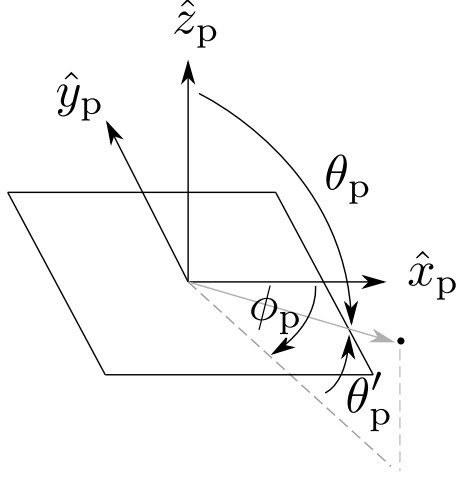


Figure 7: Detector's boresight in cartesian and polar coordinate

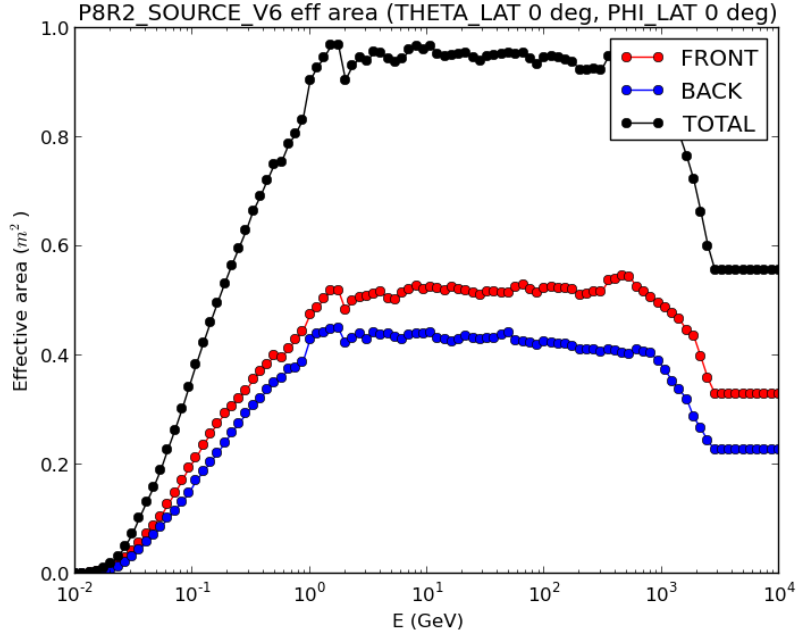


Figure 8: Effective area of Fermi-LAT

why parallel computation fit really well to this problems. To maximize all of the threading process in the cluster, master-slave technique has been applied to get rid of the idle thread to maximize our resource of computation.



### 3.4 Interaction model

Incident proton spectrum in rigidity could be represent as  
**Single power law (SPL)**

$$\frac{dN}{dR} = R_0 R^{-\gamma} \quad (8)$$

**Broken power law (BPL)**

$$\frac{dN}{dR} = \begin{cases} R_0 R^{-\gamma_1} & : E < E_{\text{Break}} \\ R_0 [R(E_{\text{Break}})]^{\gamma_2 - \gamma_1} R^{-\gamma_2} & : E \geq E_{\text{Break}} \end{cases} \quad (9)$$

In this work, we use the scattering amplitude from hadronic collision [12] that could produce a photon as a secondary product that could be detected by *Fermi*-LAT.

$$\frac{dN_\gamma}{dE_\gamma} \propto \int_{E_\gamma}^{E_{\text{max}}} dE' \frac{dN_p}{dE'} \frac{d\sigma^{pp \rightarrow \gamma}(E', E_\gamma)}{dE_\gamma} \quad (10)$$

The atmospheric composition already known well enough that mostly combined with nitrogen gas as well as oxygen molecules [13]. In order to get scattering amplitude from proton-proton collision we treat a crossection of single hadronic collision with a fraction of nitrogen atom which is almost equal to oxygen atom [14] at relativistic level of kinetic energy.

In 2015, the direct measurement of Helium spectrtum has been done by using AMS-02 in [15]. Improvement of model precision was included by taking into account incident of Helium cosmic ray particle as a first order correction and please note that we ignore other heavier atom.

$$\frac{dN_\gamma}{dE} \propto \sum_{E_{\text{inc},i}} \left[ \frac{E_{\text{inc},i}}{E_{\gamma,i}} \Delta(E_{\text{inc},i}) \right] \left[ f_{pp} \frac{dN_{\text{H}}}{dE_{\text{inc},i}} \left\{ 1 + \frac{\sigma_{\text{HeN}}}{\sigma_{pN}} \left( \frac{dN_{\text{H}}}{dR} \right)^{-1} \frac{dN_{\text{He}}}{dR} \frac{dR_{\text{He}}}{dR_{\text{H}}} \right\} \right] \quad (11)$$

where

- Red color terms is an **incident proton spectrum** as in Eq (8, 9)
- Use **helium spectrum from AMS-02 measurement (2015)**
- $f_{pp} \equiv E_\gamma (d\sigma^{ij \rightarrow \gamma} / dE_\gamma)$  is a table in K&O model which behave like a scattering amplitude that depend on the energy of incident particle
- Crossection  $\sigma_{\text{HeN}} / \sigma_{pN}$  at energy more than 10 GeV is approximately plateau ( $\approx 1.6$ )

### 3.5 Optimization

**Poisson likelihood function** define as Eq 12

$$\mathcal{L} = \prod_{i=1}^N P_{\text{pois}}(n_{i,\text{model}}, n_{i,\text{measurement}}) \quad (12)$$

Since our spectrum order is in different order of magnitude, then the better way to define an objective function is to redefine a likelihood as a log-likelihood function for numerically convenient like Eq 13.

$$Sum = \sum_{i=1}^N -\log P_{\text{pois}}(n_{i,\text{model}}, n_{i,\text{measurement}}) \quad (13)$$

In order to get a best fit spectral indices, we do an optimization with a proper trial parameters for take gradient descent from Poisson loss function between model spectrum and flux from measurement as Figure 9

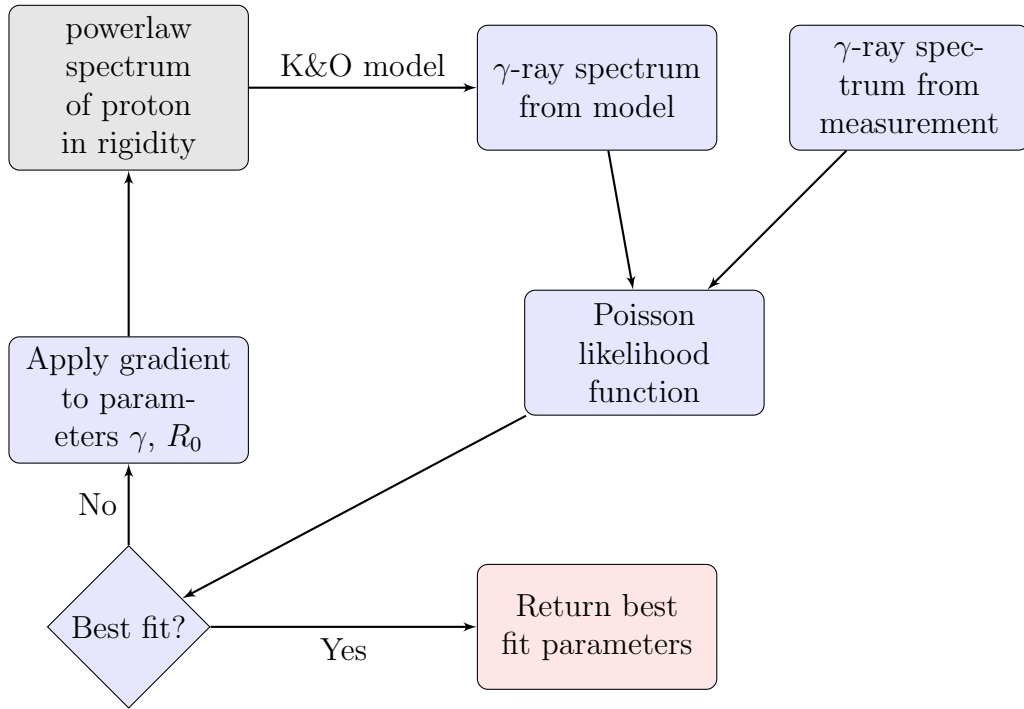


Figure 9: Flow chart of optimization process

### 3.6 Monte Carlo Simulation

In this section, we perform a brute force method to find an error of any parameters (spectral indices and break point energy). For a **statistical error (random error)**, we rerandom a counts on each bin by poisson random generator and

recalculate the flux after that optimize it as the Fig 9 do. The process of this algorithm has shown in Fig 10. The amount of simulation process require an enough number of sampling to fill up the optimized parameters and see the shape of gaussian distribution curve looks obvious enough which our work done is roughly 2000 sampling.

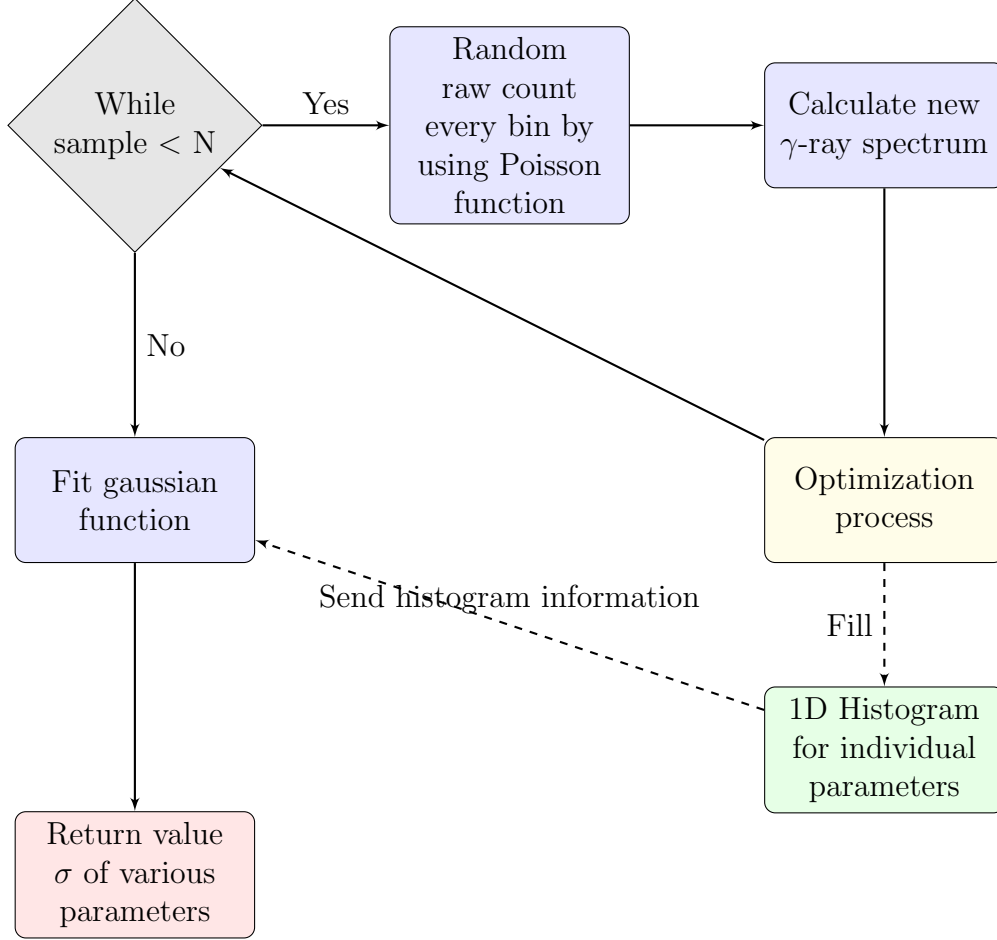


Figure 10: Flow chart of Monte Carlo simulation for statistical error

For **total error**, we also take into account error from instrument which is LAT that depends on energy. We exactly the same as the statistical error determination but one more thing that including to this algorithm is to pick three energy bin (10, 100, 1000 GeV) then rerandom flux in these three bin and apply a cubic spline interpolation to smooth the line for a statistical reason [10]. The demonstration of this program is shown as Fig 11.

### 3.7 Likelihood ratio test (LRT)

In order to determine significant level between null model and alternative model, we use Wilk's theorem [16]. Basically, this method is to regard a given

likelihood

$$\mathcal{L} \equiv \prod_{\alpha=1}^n f(x_{\alpha}, \theta_1, \theta_2, \dots, \theta_h) \quad (14)$$

where

- $x_{\alpha}$  is represent a variant from model and data
- $\theta_i$  is a degree of freedom (DOF)

The explicit declaration with an obvious method to implement has been proved in [17] as the Eq 15

$$\text{LRT} = -2 \ln \left( \frac{\mathcal{L}_{\text{null}}}{\mathcal{L}_{\text{alternative}}} \right) \quad (15)$$

## 4 Preliminary Results

### Count map and distribution

First step to check whether data that have in our hand is makes some sense or not is to simply plot the distribution of photon from a picked single weekly photon file as in Fig 12. Another step is to see the histogram of photon over energy as 13.

### Exposure maps

This step require a lot of effort to make it robust and many of testing has been performed from the serial to parallel code along the way of development. To overview some of the exposure map, the selected four out of fifty exposure map has shown in the Fig (14, 15) in cartesian and polar plot sequentially.

### Differential Flux of $\gamma$ -ray

Lastly, preliminary of gamma-ray spectrum has been computed and show in Fig 16.

## 5 Research planning

Task\Timing	Jan 2020	Feb 2020	Mar - July 2020	Aug 2020
Extract limb's gamma-ray				
Statistical Testing				
SPC 2020				
Writing Thesis				
Thesis Defense				

Table 1: Timeline

## References

- [1] V. F. Hess (The Nobel Foundation, 1936).
- [2] D. Pacini, Il Nuovo Cimento **3**, 93 (1912), URL <https://doi.org/10.1007/BF02957440>.
- [3] J. Clay, Proceedings of the Section of Sciences, Koninklijke Akademie van Wetenschappen te Amsterdam **30**, 1115 (1927).
- [4] O. Adriani, G. C. Barbarino, G. A. Bazilevskaya, R. Bellotti, M. Boezio, E. A. Bogomolov, M. Bongi, V. Bonvicini, S. Borisov, S. Bottai, et al., The Astrophysical Journal **765**, 91 (2013), URL <http://stacks.iop.org/0004-637X/765/i=2/a=91>.
- [5] M. Aguilar (AMS Collaboration), Phys. Rev. Lett. **114**, 171103 (2015), URL <https://link.aps.org/doi/10.1103/PhysRevLett.114.171103>.
- [6] S. Swordy, Space Science Reviews **99**, 85 (2001), ISSN 1572-9672, URL <https://doi.org/10.1023/A:1013828611730>.
- [7] A. A. Abdo, M. Ackermann, M. Ajello, W. B. Atwood, L. Baldini, J. Ballet, G. Barbiellini, D. Bastieri, B. M. Baughman, K. Bechtol, et al. (Fermi-LAT Collaboration), Phys. Rev. D **80**, 122004 (2009), URL <https://link.aps.org/doi/10.1103/PhysRevD.80.122004>.
- [8] M. Ackermann, M. Ajello, A. Albert, A. Allafort, W. B. Atwood, M. Axelsson, L. Baldini, J. Ballet, G. Barbiellini, D. Bastieri, et al., The Astrophysical Journal Supplement Series **203**, 4 (2012), URL <http://stacks.iop.org/0067-0049/203/i=1/a=4>.
- [9] M. Ackermann, M. Ajello, A. Albert, A. Allafort, L. Baldini, G. Barbiellini, D. Bastieri, K. Bechtol, R. Bellazzini, R. D. Blandford, et al. (Fermi LAT Collaboration), Phys. Rev. Lett. **112**, 151103 (2014), URL <https://link.aps.org/doi/10.1103/PhysRevLett.112.151103>.
- [10] M. Ackermann, M. Ajello, A. Albert, A. Allafort, W. B. Atwood, M. Axelsson, L. Baldini, J. Ballet, G. Barbiellini, D. Bastieri, et al., The Astrophysical Journal Supplement Series **203**, 4 (2012), URL <http://stacks.iop.org/0067-0049/203/i=1/a=4>.

- [11] W. Atwood et al. (Fermi-LAT) (2013), 1303.3514, URL <http://inspirehep.net/record/1223837/files/arXiv:1303.3514.pdf>.
- [12] M. Kachelrieß and S. Ostapchenko, Phys. Rev. D **86**, 043004 (2012), URL <https://link.aps.org/doi/10.1103/PhysRevD.86.043004>.
- [13] J. M. Wallace and P. V. Hobbs, *Atmospheric* (Science, 2006).
- [14] T. W. Atwater and P. S. Freier, Phys. Rev. Lett. **56**, 1350 (1986), URL <https://link.aps.org/doi/10.1103/PhysRevLett.56.1350>.
- [15] M. Aguilar, D. Aisa, B. Alpat, A. Alvino, G. Ambrosi, K. Andeen, L. Arruda, N. Attig, P. Azzarello, A. Bachlechner, et al. (AMS Collaboration), Phys. Rev. Lett. **115**, 211101 (2015), URL <https://link.aps.org/doi/10.1103/PhysRevLett.115.211101>.
- [16] S. S. Wilks, Ann. Math. Statist. **9**, 60 (1938), URL <https://doi.org/10.1214/aoms/1177732360>.
- [17] J. P. Huelsenbeck and K. A. Crandall, Annual Review of Ecology and Systematics **28**, 437 (1997), <https://doi.org/10.1146/annurev.ecolsys.28.1.437>, URL <https://doi.org/10.1146/annurev.ecolsys.28.1.437>.

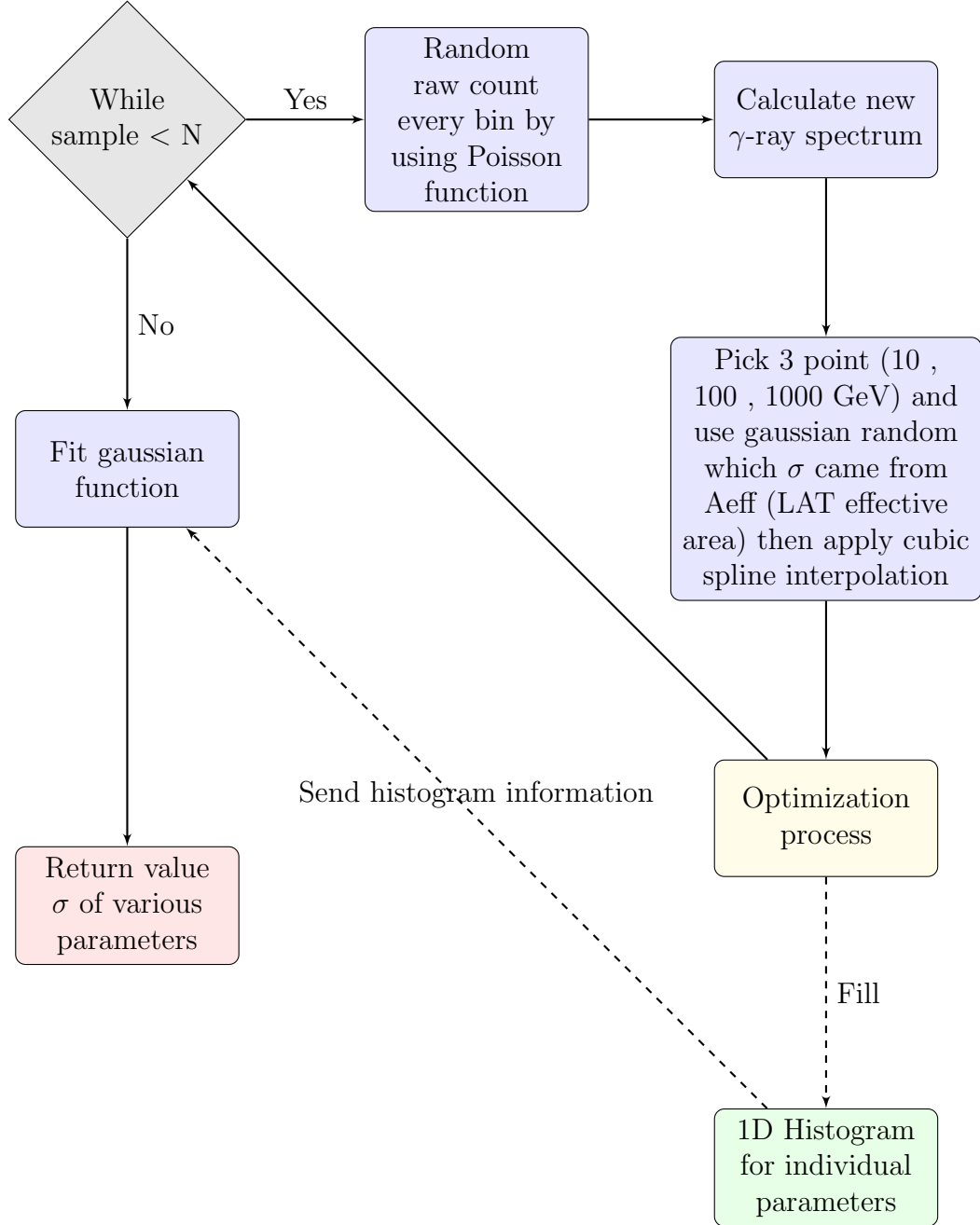


Figure 11: Flow chart of Monte Carlo simulation for total error

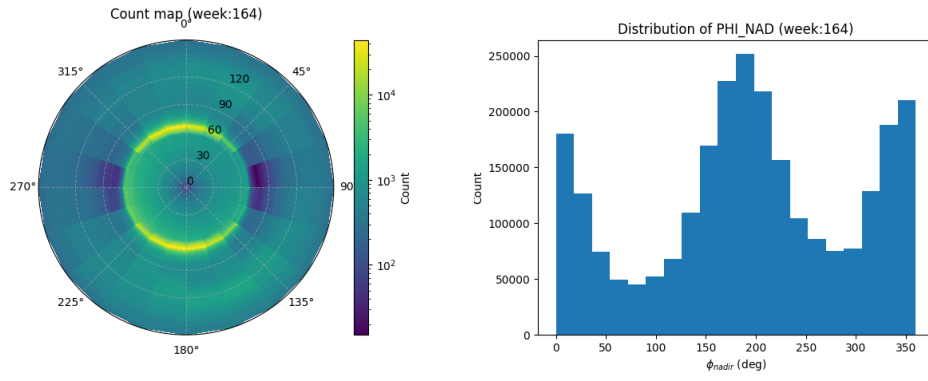


Figure 12: An example distribution of  $\gamma$ -ray from a single week

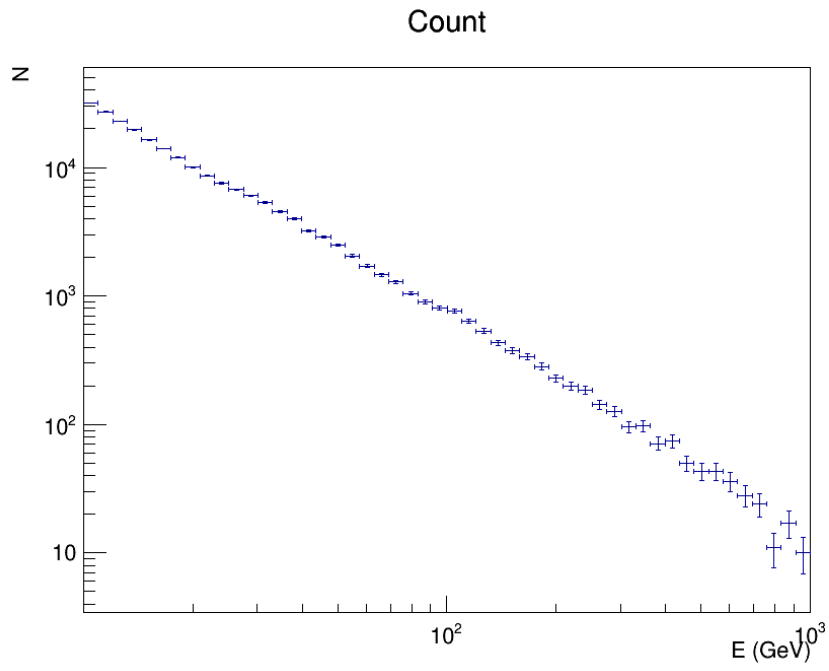


Figure 13: Raw histogram of photon in energy



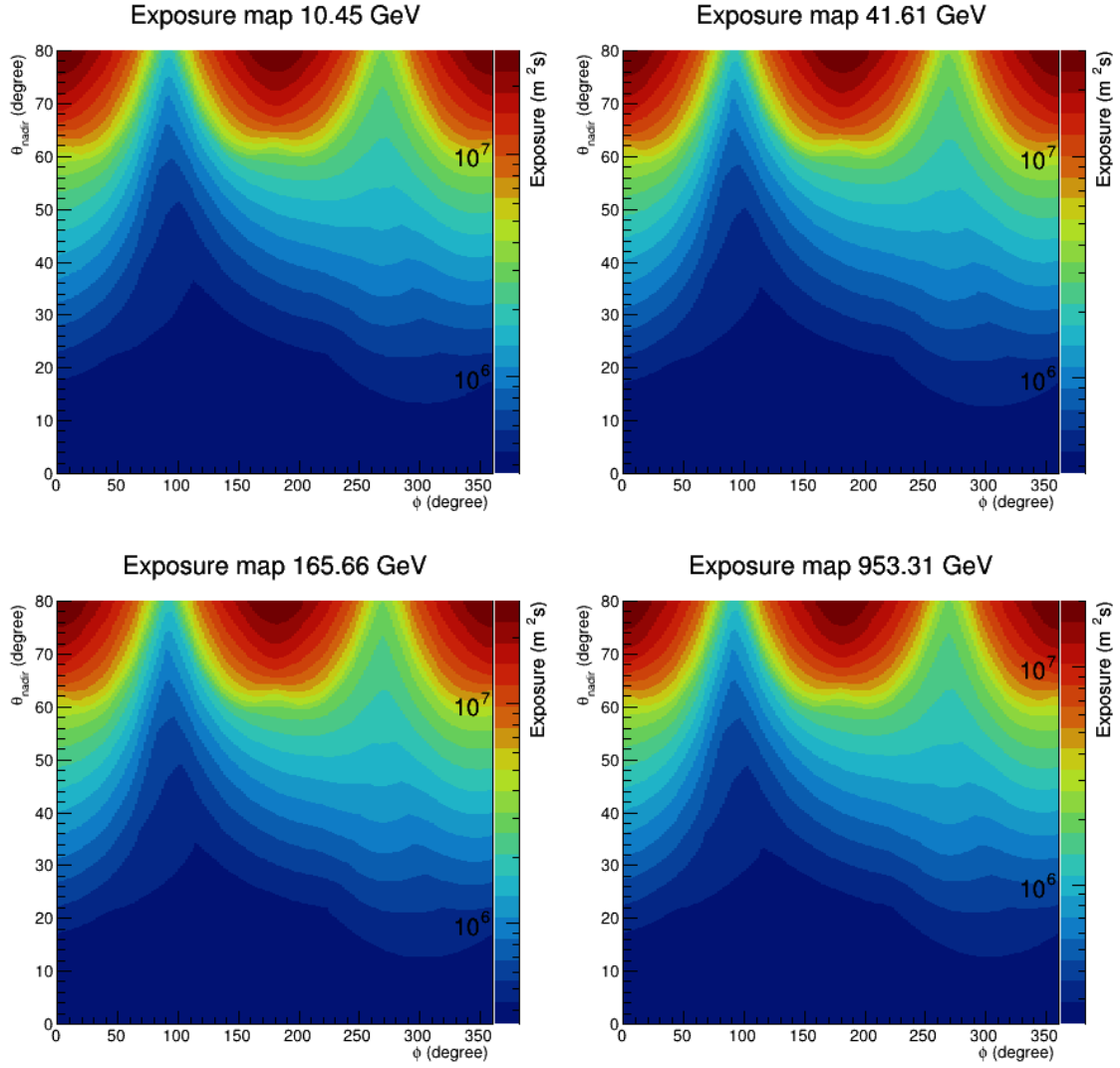


Figure 14: Exposure map of various  $\gamma$ -ray energy in cartesian plot

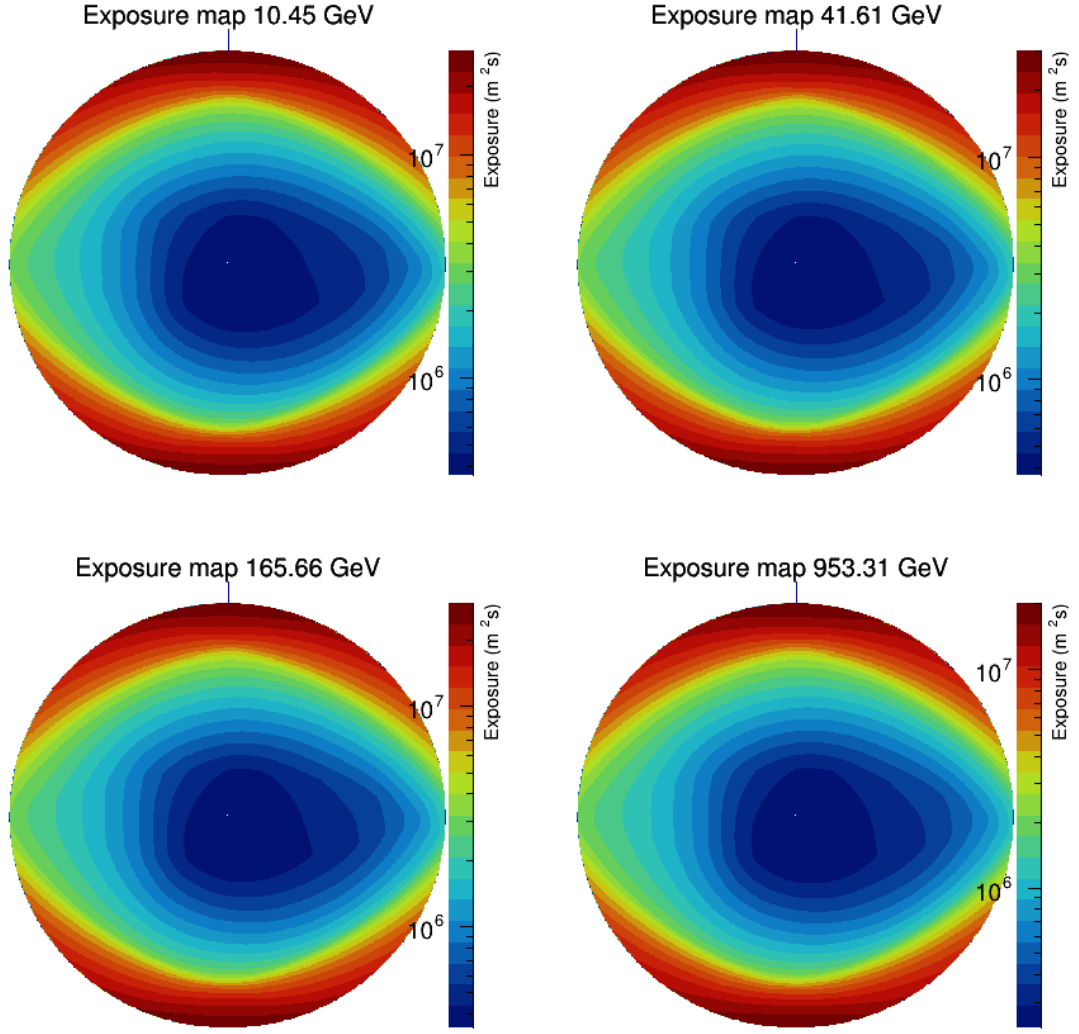


Figure 15: Exposure map of various  $\gamma$ -ray energy in polar plot

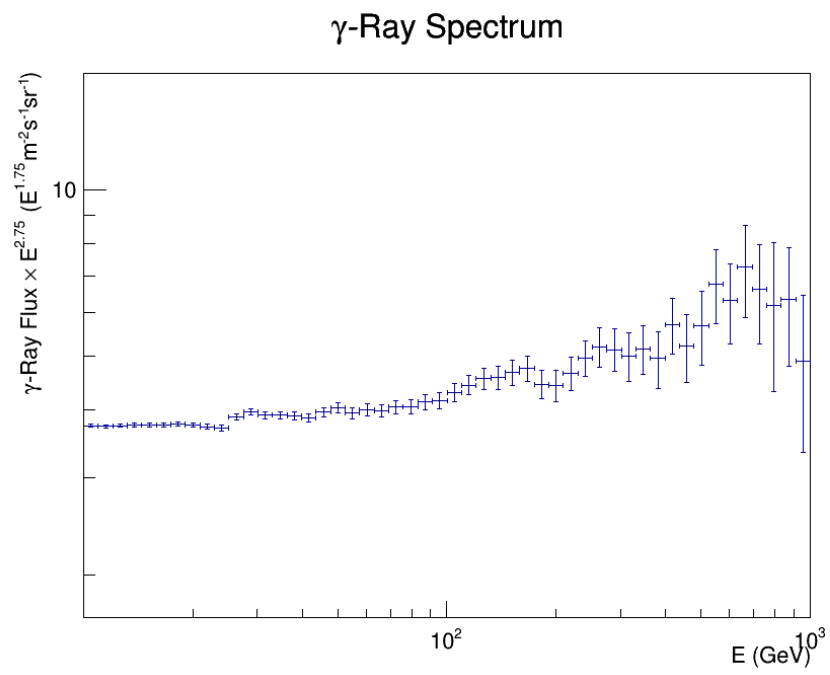


Figure 16:  $\gamma$ -ray spectrum in energy